Applied Physics Letters ARTICLE pubs.aip.org/aip/apl

Time-multiplexing single-photon imaging lidar with single-pixel detector

Cite as: Appl. Phys. Lett. **124**, 051104 (2024); doi: 10.1063/5.0187820
Submitted: 16 November 2023 · Accepted: 9 January 2024 ·
Published Online: 30 January 2024

Mingjia Shangguan,[a] Yayun Liang, Ye Li, and Yican Mo

AFFILIATIONS

State Key Laboratory of Marine Environmental Science, College of Ocean and Earth Sciences, Xiamen University, Xiamen 361102, China

[a]Author to whom correspondence should be addressed: mingjia@xmu.edu.cn

ABSTRACT

A time-multiplexing technique is proposed and demonstrated for single-photon imaging lidar, utilizing a large-area single-pixel single-photon detector to simultaneously detect the multi-pixel echoes. In this time-division multiplexing lidar, the echo signals from different pixels of the fiber array are delayed through fibers of varying lengths, merged into a fiber bundle, and then sequentially detected by the large-area single-pixel detector. In the experimental demonstration, a two-detector system capable of imaging 122 pixels using single-photon imaging lidar was showcased in three-dimensional imaging. Furthermore, the spectral broadening caused by multimode fiber dispersion was analyzed. Imaging of four different targets at a distance of 80 m was experimentally validated. This time-multiplexing technique can greatly reduce the number of single-photon detectors required in imaging lidar systems, making it suitable for low-cost lidar applications.

Lidar technology has experienced rapid development in various fields such as atmospheric and oceanic remote sensing,[1,2] laser mapping,[3] greenhouse gas monitoring,[4] and autonomous driving.[5] One key advancement in lidar is the incorporation of single-photon detectors, enabling long-range measurements with low-power lasers and small aperture optical receivers.[6–10]

To achieve three-dimensional (3D) imaging with single-photon lidar, the most commonly employed approach involves the use of mechanical scanners or optical phased arrays for beam scanning.[11,12] However, this approach sacrifices imaging time. To achieve faster imaging speed, an alternative approach has been proposed, which involves the utilization of multiple laser beams and multiple pixel detectors.[13,14] For instance, the Lunar Orbiter Laser Altimeter (LOLA) utilizes a five-beam configuration,[15,16] while the ICESat-2 Advanced Topographic Laser Altimeter System (ATLAS) employs a six-beam configuration.[3] Taking advantage of the low energy requirements of single-photon lidar, a multi-beam photon-counting lidar system with 100 beams and a 100-channel single-photon avalanche diode (SPAD) detector has been proposed.[17,18] This system not only achieves a larger field of view (FOV), but also enables reliable identification and removal of noise events.[17] However, the use of a large number of laser beams and multi-channel SPAD detectors introduces complexity to the system. Additionally, the maturity of SPAD array technology has paved the way for the proposal of single-photon lidar based on SPAD arrays. However, these instruments always cost a lot due to the difficulty in the fabrication of the single-photon detector array with highly integrated numerous pixels of balanced detection efficiency and noise level.[19–21]

To address these challenges, researchers have proposed a solution based on frequency-division multiplexing[22] and a combined wavelength-division multiplexing and time-division multiplexing beamforming scheme.[23] By employing these two techniques, namely, utilizing lasers with different repetition frequencies or multiplexing with different wavelengths, it becomes possible to implement a multi-beam lidar system using only a single-pixel single-photon detector as the receiver. In this Letter, we propose enabling imaging capabilities in a conventional single-pixel lidar setup, typically consisting of a single-wavelength laser, a single-pixel detector, and a single-channel time-to-digital converter (TDC), without scanning, by employing the time-division multiplexing technique. Compared to multi-wavelength imaging systems, the use of a single laser wavelength allows the optical receiver to suppress background radiation noise from different pixels with a single-band filter, simplifying the optical reception system. To achieve imaging, an array of optical fibers is employed at the optical reception end, where different pixels are delayed using fibers of varying lengths to separate them in the time domain. Unlike the use of optical switches to switch between different wavelengths of lasers at the lidar transmitter for time-division multiplexing,[23] this work proposes a

time-division multiplexing at the lidar receiver through optical fiber delays applied to different pixels. Subsequently, the fibers from different pixels are recombined into a fiber bundle, allowing detection by a single-pixel single-photon detector. In this regard, a large-area single-pixel single-photon detector is utilized to efficiently collect signals from the optical array. Furthermore, the spectral broadening caused by multimode fiber (MMF) dispersion was analyzed. Imaging of four different targets at a distance of 80 m was experimentally validated.

The schematic diagram of the single-photon imaging lidar system setup is illustrated in Fig. 1. The system consists of four subsystems: a 532 nm pulsed laser, a transceiver, a time-multiplexing module, and a data acquisition system. The utilization of a 532 nm wavelength laser in this lidar system is intended to accommodate its underwater imaging capabilities. The system employs a compact fiber-based picosecond (ps) laser with a master oscillator power amplifier (MOPA) architecture. The seed laser operates at a wavelength of 1064 nm and is a single-mode single-frequency pulsed laser. It undergoes amplification through a single-mode ytterbium-doped fiber amplifier (SM-YDFA) and two-stage high-power ytterbium-doped fiber amplifiers (HP-YDFAs). To generate the desired 532 nm wavelength, the laser beam passes through a lithium borate (LBO) crystal for second harmonic generation. The system achieves an average power output of up to 80 mW, and after passing through a concave lens, the beam divergence is 12 mrad. The laser pulse has a full width at half maximum (FWHM) of 95 ps. The pulse repetition rate is 1 MHz, corresponding to a non-ambiguous detection range of 150 m. Each pulse carries an energy of 80 nj.

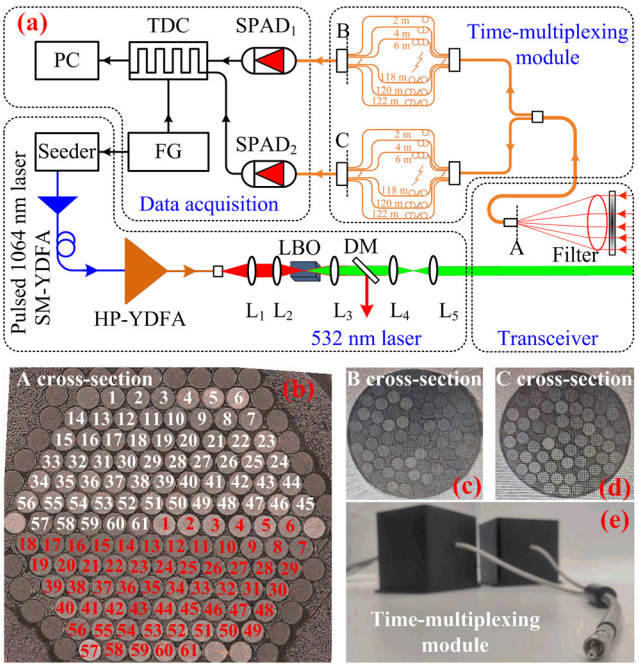

FIG. 1. (a) Schematic setup of the single-photon imaging lidar. SM-YDFA: single-mode ytterbium-doped fiber amplifier; HP-YDFA: high-power ytterbium-doped fiber amplifier; L: lens; LBO: lithium borate; DM: dichroic mirror; SPAD: single-photon avalanche diode; TDC: time-to-digital converter; FG: function generator; and PC: personal computer. (b) Enlarged cross-sectional images of the fiber optic interfaces at positions A(b), B(c), and C(d) as marked in (a), along with (e) a photograph of the time-division multiplexing module.

To achieve a miniaturized structure, an all-fiber connection configuration is employed in the optical receiver system of the single-photon imaging lidar. The backscattered signal generated by the interaction between the 532 nm laser and the target is collected through a large-beam achromatic fiber collimator with a focal length of 80 mm. A 50 mm diameter narrowband filter with a bandwidth of 0.5 nm is placed in front of the collimator, and its center wavelength matches the laser wavelength. After passing through this collimator, the backscattered signal is coupled into a fiber array composed of 122 MMFs, each with a mode field diameter of 50 μm and a numerical aperture (NA) of 0.22. The cross section of the fibers at position A, marked in Fig. 1(a), is shown in Fig. 1(b), with numbering from 1 to 61 in two sets, sequentially adjacent for each number. The pixels with different numbers are delayed using fibers of varying lengths, with the fiber length increasing by 2 m for each pixel. Considering the refractive index of the fiber, this results in a delay increase in ~10 ns for each pixel. The fiber corresponding to number 61 has a delay fiber length of 122 m, corresponding to a delay of 610 ns.

To optimize the fill factor, the 50/55/65 μm (core/cladding/coating) MMFs underwent a coating layer removal process and were subsequently arranged in a well-organized manner, as illustrated in Figs. 1(b)–1(d). As a result, the fill factor reaches 83%. Additionally, due to its fiber array structure, the isolation level between pixels exceeds 100 dB, providing a significant advantage compared to SPAD array detectors. The total diameter of the fiber cluster formed by the 122-fiber array is limited to within 0.72 mm, corresponding to a FOV of 9 mrad for the lidar system. Each fiber corresponds to a FOV of 0.625 mrad, and at a target distance of 80 m in the experiment, the corresponding lateral resolution is ~8.5 cm, additionally considering the effective aperture of the receiving telescope, which is 3.5 cm. The transmitted laser and the receiving collimator are in close proximity, and the geometric overlap factor, representing the ratio of the laser beam overlapping with the FOV of the receiver, reaches 100% at a distance of ~2 m. Subsequently, the two sets of fibers numbered 1–61 are individually merged into their respective fiber clusters. The fiber clusters exhibit a transmission diameter of ~500 μm, and the cross sections of the fibers at positions B and C are depicted in Figs. 1(c) and 1(d), respectively. The photograph of the entire time-multiplexing module is shown in Fig. 1(e).

The signals from the two sets of 61-pixel points output by the time-multiplexing module are detected in a time-division manner using their respective single-pixel SPAD detectors. The detection efficiency of the SPAD is 52% at 532 nm, accompanied by a dark count rate of 100 counts per second (cps) and a saturation count rate of 40 MHz. As single-photon detectors have evolved from detecting a single pixel to simultaneously capturing 61 pixels, there has been a substantial increase in the number of detected photons. Fortunately, the implementation of the time-division multiplexing technique enables the temporal separation of photons from various pixels. This not only prevents the detector from saturating due to the rapid surge in photons but also significantly enhances the utilization efficiency of the single-photon detector without sacrificing detection efficiency.

As to the electronic module, a homemade function generator (FG) based on the field programmable gate array (FPGA) provides precise control signal for laser and the TDC. A high-precision TDC

(Swabian Instruments, Time Tagger Ultra) with root mean square (rms) jitter of 9 ps is adopted to record the time of pulse emission and photon detection.

To analyze the effectiveness of time-division multiplexing, measurements were conducted using the lidar system to capture echoes from a white plane placed at the lidar's output port. The sampling interval of the lidar was set to 50 ps, and the accumulation time was set to 1 s. The temporal distribution of the received signals from the 61 pixels is shown in Fig. 2(a). For convenient statistical analysis, the peaks of the 61 signals were normalized to their respective peak values. From the figure, it can be observed that the time delay between adjacent pixels is ~10 ns, which is determined by the length differences of the delay MMFs. The peaks exhibit a relatively uniform distribution in the time domain, although slight variations can be attributed to the differences in fiber lengths.

Furthermore, as depicted in Fig. 2(b), with increasing delay, the extracted waveforms become broader. The statistical analysis of the width of the 61-pixel waveforms is presented in Fig. 2(c), revealing that for every additional meter of MMF, there is an approximate increase in 15 ps in waveform width. This broadening is primarily attributed to the dispersion of the pulsed 532 nm laser introduced by the MMF.[24] In the absence of broadening, specifically for the first pixel, the width of the waveform (τ_{lidar}) obtained from single-photon imaging lidar measurements was 1.32 ns, primarily determined by the temporal resolution of the time-to-digital converter (τ_{TDC}, 10 ps), the laser pulse duration (τ_{laser}, 95 ps), the timing jitter of the single-photon avalanche diode (τ_{spad}, 1.3 ns), and the time jitter of the synchronous signal (τ_{syn}, 10 ps). The width, τ_{lidar}, was calculated using the formula $\tau_{lidar} = (\tau_{TDC}^2 + \tau_{laser}^2 + \tau_{spad}^2 + \tau_{syn}^2)^{0.5}$, resulting in a value of 1.32 ns, which correlates with the measured value.

To assess the variations in the peak position extraction among different pixel locations, the above-mentioned experiment was repeated 60 times. The average and standard deviation of the center positions of each pixel location were calculated from the 60 sets of data, as shown in Fig. 3. To reduce random errors in the single-photon data, we applied a 1 ns sliding window during the data processing before extracting the peak positions using the "findpeaks" MATLAB function.

From the figure, it can be observed that, although the pixel points with larger delays, as shown in Fig. 2, exhibit wider waveform widths, the precision of peak extraction remains relatively high. Despite an increase in the standard deviation with increasing delay, the standard deviation of peak positions extracted from the 61st pixel, compared to the first pixel, only increases from 0.5 to 0.8 cm.

To demonstrate the effectiveness of the time-multiplexing-based single-photon lidar, imaging experiments were conducted on four different targets at a distance of 80 m, including a planar wall, an inclined wall, a step, and a stripe. Figure 4 illustrates the typical distribution of reference and target signals detected by $SPAD_1$ with a bin width of 50 ps and an accumulation time of 1 s. The target is an inclined wall located at a distance of 80 m, while the reference signals originate from a white plane placed at the lidar's output port. From the reference signals, it is evident that the intensity varies for each pixel, and as the length of the optical fiber increases, resulting in larger delays at pixel points, the signal generally weakens. When examining the signals reflected from the target, as shown in Fig. 4(b), the delay of each target pixel relative to its corresponding reference pixel represents the target's distance, and variations in the reflectivity of the target corresponding to different pixels result in an uneven intensity distribution. Moreover, in this study, employing 61 pixels spanning ~610 ns in the time domain and considering a detection distance of 80 m, this leads to the occurrence of target signals with return times exceeding 1 μs in the earlier half of the time axis, as depicted in Fig. 4(b). From the signals in Fig. 4, it can be observed that variations in the photon counts of the lidar signal, influenced by the target's reflectivity, impose greater requirements on the dynamic measurement range of the lidar system. In this work, the lidar has a measurement dynamic range of ~40 dB, which is adequate for detecting targets with relatively minor variations in reflectivity. However, when it comes to detecting more complex targets, it will be essential to implement techniques to extend the dynamic range, such as the fast-gated single-photon counting technique.[25] The lidar emitted 10^6 laser pulses within one second, and the accumulated photon counts on each pixel were less than 6×10^4 photons. This implies that in this experiment, the detection of photons on each pixel was less than 0.06 per pulse, which is lower than the saturation photon

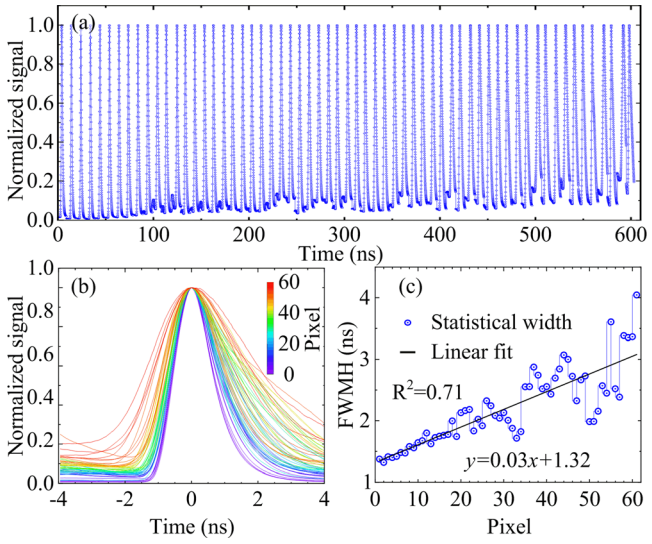

FIG. 2. (a) Temporal distribution of the 61-pixel points, normalized to their respective peaks. (b) Extracted waveforms of the echo signals from the 61 pixels in (a), with the peak positions aligned at 0 s. (c) Statistical analysis of the waveform width for different pixels.

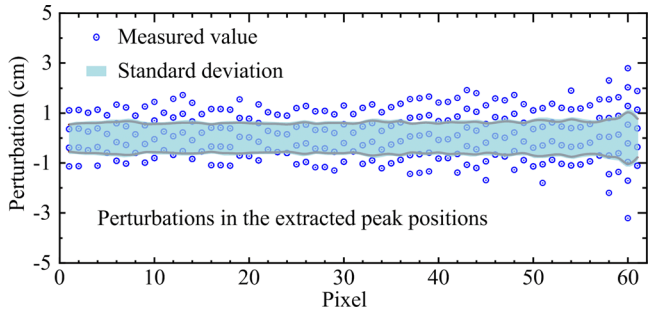

FIG. 3. Perturbations in the extracted peak values for the 61 pixels, presenting the statistical results of 60 measurements.

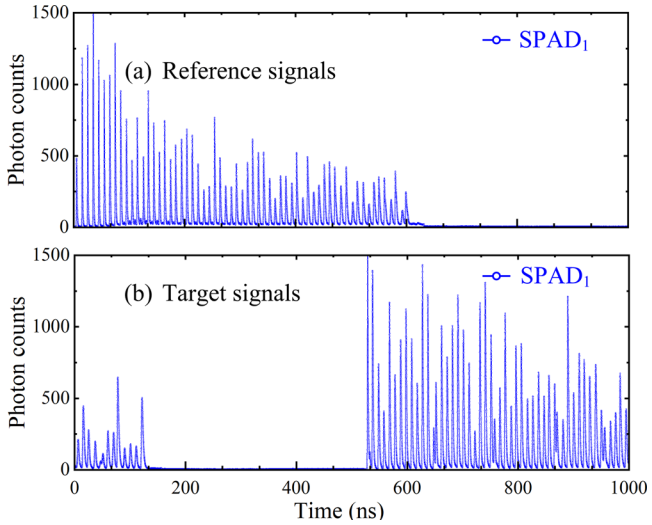

FIG. 4. Typical distribution of reference and target signals from $SPAD_1$.

count for the single-photon detector. Consequently, despite variations in the signal intensity among different pixels in this work, it remains feasible to extract the waveforms corresponding to different pixels.

As shown in Fig. 5, the lidar achieved imaging of four targets with different shapes at a distance of 80 m without scanning, using only two single-pixel detectors and two-channel TDC. The

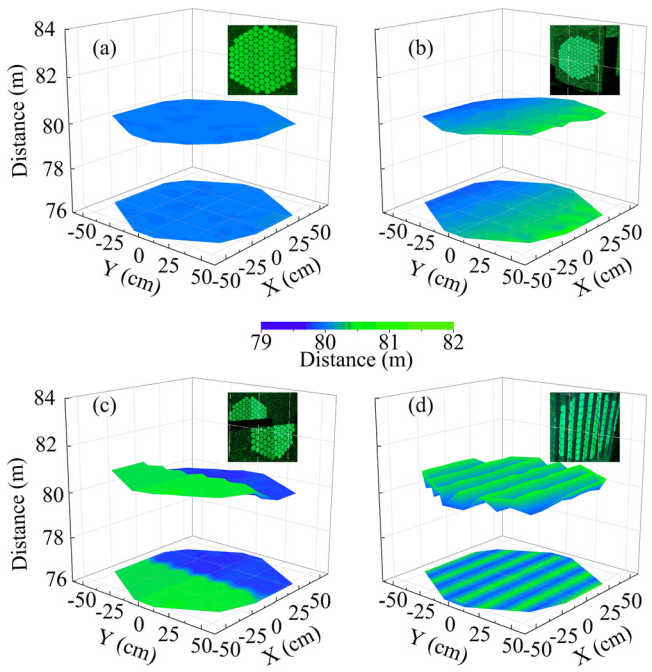

FIG. 5. Imaging of planar (a), inclined surface (b), step (c), and stripe (d) using the single-photon imaging lidar, with experimental photographs in the top right corner of each subfigure showing images captured by illuminating the target with different pixels.

experiments were conducted in the playground of Xiamen University. Additionally, due to the strong solar radiation at 532 nm during the daytime and the limited bandwidth of the filters, the experiments were conducted at night. By analyzing the depth data of the flat wall in Fig. 5(a), it was observed that the 122 pixels detected distances within a range of 80 m ± 2.5 cm, indicating that the lidar system attained an approximate 5-cm distance resolution at a distance of 80 m. In this work, although imaging detection was demonstrated with only 122 pixels, it validates the capability of single-pixel detectors and single-channel TDC to achieve 61 pixels. In the future, by designing more complex fiber arrays, it will significantly reduce the number of single-photon detectors and the channels of high-speed TDCs.

In conclusion, a fiber-based single-photon imaging lidar technology was proposed and demonstrated using a time-multiplexing technique without scanning devices. The scheme enables imaging capabilities in a conventional single-pixel lidar setup, typically consisting of a single-wavelength laser, a single-pixel detector, and a single-channel TDC, without scanning, by employing the time-division multiplexing technique. By employing a regularly arranged fiber array at the receiver end, the echo signals from different pixels were delayed using fibers of different lengths. These delayed signals were then combined into a new fiber cluster and detected by a single-pixel single-photon detector. In this Letter, the dispersion caused by the MMFs used for delay was analyzed. Furthermore, the feasibility of the proposed technique was validated through the detection of four different-shaped targets at a distance of 80 m. The technique offers several advantages. First, the high isolation between fibers in the fiber array significantly reduces interference between pixels. Second, the use of a single wavelength for imaging different pixels enables the application of the same set of filtering devices, resulting in the high signal-to-noise ratio for echo signal extraction. Finally, the system requires only a single readout circuit, allowing for high-speed imaging.

In the future, measures will be taken to enhance the performance of this lidar system. These measures include improving algorithms and hardware to enable simultaneous detection of multiple targets within the FOV, as well as applying the system for detecting underwater targets in environments with strong absorption and scattering backgrounds. Furthermore, near-infrared laser sources and narrower filtering techniques will be employed to achieve the capability of the imaging lidar to operate continuously throughout the day for targets in the atmosphere. Finally, the time-multiplexing technique can be easily implemented in existing multi-beam lidar systems, demonstrating the significant potential of multi-beam lidar applications.

This work was supported by the National Key Research and Development Program of China (No. 2022YFB3901704), the Innovation Program for Quantum Science and Technology (No. 2021ZD0303102), the Fujian Provincial Central Guided Local Science and Technology Development Special Project (No. 2022L3078), the Joint Funds of the National Natural Science Foundation of China (No. U2106210), the National Science Foundation of Fujian Province of China (No. 2020J01026), and the MEL-RLAB Joint Fund for Marine Science & Technology Innovation.

AUTHOR DECLARATIONS

Conflict of Interest

The authors have no conflicts to disclose.

Author Contributions

Mingjia Shangguan: Conceptualization (lead); Data curation (equal); Funding acquisition (lead); Investigation (equal); Supervision (lead); Writing – original draft (lead); Writing – review & editing (lead). **Yayun Liang:** Data curation (equal). **Ye Li:** Investigation (equal). **Yican Mo:** Investigation (supporting).

DATA AVAILABILITY

The data that support the findings of this study are available from the corresponding author upon reasonable request.

REFERENCES

[1]C. Yu, M. Shangguan, H. Xia, J. Zhang, X. Dou, and J.-W. Pan, Opt. Express **25**(13), 14611 (2017).
[2]J. H. Churnside and J. A. Shaw, Appl. Opt. **59**(10), C92 (2020).
[3]W. Abdalati, H. J. Zwally, R. Bindschadler, B. Csatho, S. L. Farrell, H. A. Fricker, D. Harding, R. Kwok, M. Lefsky, and T. Markus, Proc. IEEE **98**(5), 735 (2010).
[4]S. Yu, Z. Zhang, H. Xia, X. Dou, T. Wu, Y. Hu, M. Li, M. Shangguan, T. Wei, and L. Zhao, Light Sci. Appl. **10**(1), 212 (2021).
[5]S. Royo and M. Ballesta-Garcia, Appl. Sci. **9**(19), 4093 (2019).
[6]M. Shangguan, Z. Yang, M. Shangguan, Z. Lin, Z. Liao, Y. Guo, and C. Liu, Appl. Opt. **62**(19), 5301 (2023).
[7]M. Shangguan, Z. Liao, Y. Guo, and Z. Lee, Opt. Express **31**(16), 25398 (2023).
[8]M. Shangguan, H. Xia, C. Wang, J. Qiu, G. Shentu, Q. Zhang, X. Dou, and J-w Pan, Opt. Express **24**(17), 19322 (2016).
[9]M. Shangguan, H. Xia, C. Wang, J. Qiu, S. Lin, X. Dou, Q. Zhang, and J.-W. Pan, Opt. Lett. **42**(18), 3541 (2017).
[10]M. Shangguan, Z. Yang, Z. Lin, Z. Lee, H. Xia, and Z. Weng, IEEE Geosci. Remote Sens. Lett. **20**, 1501905 (2023).
[11]A. M. Pawlikowska, A. Halimi, R. A. Lamb, and G. S. Buller, Opt. Express **25**(10), 11919 (2017).
[12]Y. Li, B. Chen, Q. Na, Q. Xie, M. Tao, L. Zhang, Z. Zhi, Y. Li, X. Liu, X. Luo, G. Lo, F. Gao, X. Li, and J. Song, Photonics Res. **9**(12), 2511 (2021).
[13]D. Shin, F. Xu, D. Venkatraman, R. Lussana, F. Villa, F. Zappa, V. K. Goyal, F. N. Wong, and J. H. Shapiro, Nat. Commun. **7**(1), 12046 (2016).
[14]S. Jahromi, J.-P. Jansson, and J. Kostamovaara, Opt. Express **24**(19), 21619 (2016).
[15]H. Araki, S. Tazawa, H. Noda, Y. Ishihara, S. Goossens, S. Sasaki, N. Kawano, I. Kamiya, H. Otake, J. Oberst, and C. Shum, Science **323**(5916), 897 (2009).
[16]P. Tarolli, Geomorphology **216**, 295 (2014).
[17]K. Y. Shrestha, W. E. Carter, K. C. Slatton, and T. K. Cossio, IEEE Trans. Geosci. Remote Sens. **50**(11), 4771 (2012).
[18]Z. Li, E. Wu, C. Pang, B. Du, Y. Tao, H. Peng, H. Zeng, and G. Wu, Opt. Express **25**(9), 10189 (2017).
[19]A. Maccarone, K. Drummond, A. McCarthy, U. K. Steinlehner, J. Tachella, D. A. Garcia, A. Pawlikowska, R. A. Lamb, R. K. Henderson, and S. McLaughlin, Opt. Express **31**(10), 16690 (2023).
[20]C. Tan, W. Kong, G. Huang, J. Hou, Y. Luo, T. Chen, X. Liu, and R. Shu, IEEE Photonics J. **14**(3), 6623407 (2022).
[21]F. Qi and P. Zhang, Opt. Express **31**(19), 30118 (2023).
[22]T. Zheng, G. Shen, Z. Li, L. Yang, H. Zhang, E. Wu, and G. Wu, Photonics Res. **7**(12), 1381 (2019).
[23]P. Hao, Z. Wang, and X. S. Yao, Opt. Lasers Eng. **164**, 107493 (2023).
[24]A. Mecozzi, C. Antonelli, and M. Shtaif, Opt. Express **20**(11), 11673 (2012).
[25]A. Tosi, A. D. Mora, F. Zappa, A. Gulinatti, D. Contini, A. Pifferi, L. Spinelli, A. Torricelli, and R. Cubeddu, Opt. Express **19**(11), 10735 (2011).